Numerical simulations of pore isolation and competition in idealized micro-spall process

Wojciech Aniszewski, Stéphane Zaleski, Antoine Llor, Leon Malan

Numerical simulations of pore isolation and competition in idealized micro-spall process

Wojciech Aniszewski[a,*], Stéphane Zaleski[a], Antoine Llor[b], Leon Malan[c]

[a] *Sorbonne Université, CNRS, Institut Jean le Rond d'Alembert, 75005 Paris, France*
[b] *CEA, DAM, DIF, 91297 Arpajon Cedex, France*
[c] *University of Cape Town, Cape Town 7701, South Africa*

Abstract

The 'micro-spall' phenomenon is a variant of fragmentation process—or spall fracture—that is traditionally discussed in context of solid materials (metals). However it concerns situations in which the medium is fully or partially *melted*—be it due to kinetic impact, detonation or laser loading. The phenomenon takes place at sub-micrometer and sub-microsecond scales making it inaccessible to direct experimental observation; so far, investigations have been restricted to observations of late time "post-mortem" fragments.

In this context, it becomes a viable approach to apply analysis using numerical description for fluids. This work presents such an application for an idealized rapid uniaxial (one-dimensional) system expansion. Cavitation in the medium is represented by including vacuous pores or cavities with surface tension whose growth and interaction are traced in time. The simulations reveal two main regimes of pore growth regulated by a characteristic Weber number.

Keywords: micro spall, cavity, Volume of Fluid (VOF), free surface, pore competition

1. Introduction

Cavitation and micro-spall (see for instance Signor et al., 2010, and references therein) appear when a weakly compressible (or expansible) liquid is suddenly submitted to a large volume growth (expansion) resulting in negative pressures. This process, which appears in many practical applications of interest, occurs when an initially solid medium is subject to an unsustained impact or detonation and is entirely or partly melted in the process. Once the system starts expanding, the pressure drop causes the onset of cavitation and pores (or bubbles filled with vapor) appear. After the initial phases of uniform expansion and pore opening, a longer-lasting phase of pore growth and competition appears, which is especially difficult to investigate either experimentally or numerically (de Rességuier et al., 2010; Signor et al., 2010).

We present here numerical simulations of this latter phase for idealized conditions relevant to micro-spall. This paper picks up on a previously published study of Malan et al. (2018) which presented low-Weber number expansions of the system (with constant expansion rates). Malan et al. (2018) focused on a *competition* phenomenon in which expansion of some of the pores caused their neighboring pores to collapse: in other words, there was a volume transfer between the pores without actual contact and merger between them. The pore competition effect is important as it is the main phenomenon driving the evolution in time of the statistical distribution of pore sizes (Everitt et al., 2006). Small pores shrink and eventually disappear as their volume is transferred to large pores. Pore statistics and pressure evolution profiles can then be obtained for future modeling purposes. Hypothetically, continued competition accompanied by coalescence could lead to formation of larger pores—or even of a single pore in the case of a spatially limited system. In this work, we focus on the practically relevant case of constant speed expansions whose rate decrease with time: the corresponding Weber numbers typically start and end respectively at ranges above and below the competition threshold.

Thus, our idealized assumptions are incompressible inviscid fluid, vanishing vapor pressure in cavities, homogeneous uniaxial "ballistic" expansion, perturbed face-centered-cubic lattice arrangement of pores. Under these assumptions, the system is characterized by a single dimensionless group, the Weber number based on the number of pores per unit volume. The "ballistic" expansion signifies evolution in which We rapidly decays: in the initial stages of expansion the flow is entirely dominated by inertia and the pores expand as if they were isolated (Ilinskii et al., 2007). As We drops the system transitions into a regime in which the bubbles interact and capillary pressure becomes significant. We investigate this transition in more detail below. Results indicate that both the uniform growth in the initial expansion phase, and the later "competition" (Everitt et al., 2006) regime can be captured.

2. Elementary characterization of ideal micro-spall

2.1. Mean expansion field

We investigate a fluid element undergoing expansion following a shock and release history. As sketched in the volume and pressure profiles of Fig. 1, pressure drops due to the accelerated

*Corresponding author. Tel: +33 1 44 27 87 14.
Email addresses: aniszewski@dalembert.upmc.fr (Wojciech Aniszewski), antoine.llor@cea.fr (Antoine Llor)
URL: http://www.lmm.jussieu.fr/~zaleski/index.html (Stéphane Zaleski)

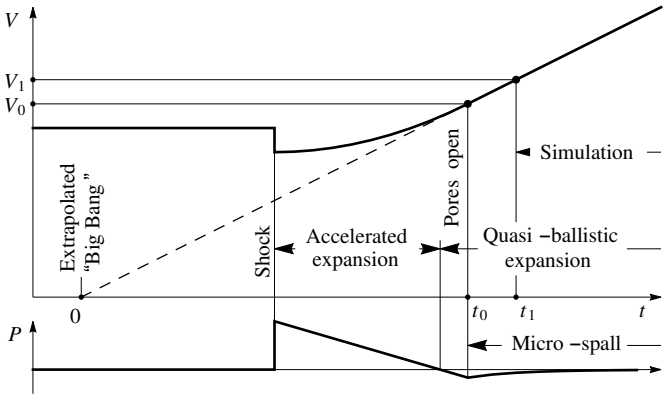

Figure 1: Sketched evolution of mean macroscopic volume and pressure of a material element undergoing mico-spall. As qualitatively represented, the initial pressure produced by the shock and the final spall stress are here assumed respectively large and small enough that the eventual expansion is nearly ballistic. This ballistic evolution can then be backward extrapolated to vanishing volume which defines the (arbitrary) time origin. As indicated, the system evolution is here simulated after pores have opened and local fluid density has returned to a nearly uniform and constant value.

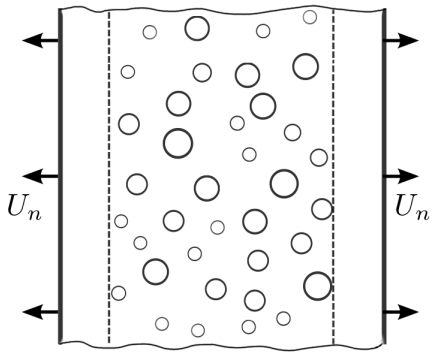

Figure 2: Schematic representation of idealized micro-spall as a pore cluster undergoing expansion along the x direction.

expansion and eventually becomes negative. At some point, the cohesive limit of the fluid is reached and pores open: in this micro-spall phase, surface tension around the pores produces a macroscopic negative stress. If this spall stress is weak enough compared to the stored momentum the system eventually evolves in a quasi-ballistic way. The micro-spall phenomenon can appear regardless of the structure of the strain tensor—which in general displays three different eigenvalues—but we shall focus here on the most common situation of uniaxial expansion and more marginally on the theoretically useful situation of isotropic expansion.

For a small enough material volume, the average strain can be considered as uniform – which corresponds e.g. to uniform laser energy distribution in laser shock-loading (Signor et al., 2010, sect. 2.2) – and the backward-extrapolated positions of all the fluid elements collapse to a single point: this is the virtual "Big Bang" that provides the time and space origins in all the following, $t = 0$ and $\mathbf{x} = \mathbf{0}$. Depending on the strain dimension and depending on the selected coordinate system, Lagrangian $\mathbf{X}$ or Eulerian $\mathbf{x}$, the mean velocity field in the material volume can always be written as

	Lagrangian	Eulerian	
Uniaxial	$\overline{u}(X,t) = \overline{u}(X,t_0) = X/t_0,$	$\overline{u}(x,t) = x/t,$	(1a)
Isotropic	$\overline{\mathbf{u}}(\mathbf{X},t) = \overline{\mathbf{u}}(\mathbf{X},t_0) = \mathbf{X}/t_0,$	$\overline{\mathbf{u}}(\mathbf{x},t) = \mathbf{x}/t,$	(1b)

where the Lagrangian coordinate $\mathbf{X}$ is the actual position at reference time t_0, while x and X represent the first coordinates of the $\mathbf{x}$ and $\mathbf{X}$ position vectors. Equations (1) describe *expansion*, as the "Hubble time" t_0 is assumed positive. The uniform but non-constant divergence of the mean velocity field is

$$\boldsymbol{\nabla} \cdot \overline{\mathbf{u}} = d/t, \tag{2}$$

where dimensionality d is 1 or 3 for respectively uniaxial or isotropic expansions, and is related to mean density through

$$\frac{\mathrm{d}}{\mathrm{d}\,t} \ln \overline{\rho} = -\boldsymbol{\nabla} \cdot \overline{\mathbf{u}}. \tag{3}$$

Combining (2) and (3) yields

$$\overline{\rho} = \overline{\rho}_0 \, (t_0/t)^d, \tag{4}$$

where the reference state is conveniently taken here at time $t = t_0$ where cavitation nuclei appear (Batchelor, 1967) and where the mean density coincides with the fluid density $\overline{\rho}_0 = \rho_l$.

Equations (1) are solutions of the Euler equation

$$\partial_t \overline{\mathbf{u}} + (\overline{\mathbf{u}} \cdot \boldsymbol{\nabla}) \overline{\mathbf{u}} = -\frac{1}{\overline{\rho}} \boldsymbol{\nabla} \overline{p}, \tag{5}$$

with zero mean pressure gradient and uniform but non-constant mean density $\overline{\rho}$. The ultimate goal of modeling is to provide a closure relationship between $\overline{\rho}$, $\overline{\mathbf{u}}$, and $\overline{p}$ so as to simulate the effect of micro-spall on large scale dynamics (possibly elliptically unstable).

2.2. *Mean pore characteristics*

At microscopic scales, micro-spall displays fluctuations on all its smooth large-scale fields. As sketched in Fig. 2, a first approximation convenient to capture surface tension effects consists in assuming all pores as spherical, with no internal mass and pressure (vanishing vapor pressure), and furthermore with identical radii $R(t)$ and no translation velocity with respect to their surroundings (Caflisch et al., 1985). Therefore, no coalescence effects can be present, and the number of pores is constant and equal to the number of cavitation nuclei at $t = t_0$. The mean number density of pores N then scales as mass density (4)

$$N = N_0 \, (\overline{\rho}/\rho_l) = N_0 \, (t_0/t)^d, \tag{6}$$

where N_0 is an initial number of cavitation nuclei. In a more realistic situation where pores may collapse (depicted in this work) or merge, this relationship does not hold.

Under the simplifying assumption of local spherical symmetry the number density of pores provides their geometric characteristics. Each pore influences a mean spherical volume defined

by the Wigner–Seitz radius $\ell(t)$ (Girifalco, 2000):

$$\frac{4\pi}{3}\ell^3 N = 1. \tag{7}$$

Seeing as the volume fraction of liquid is $(\overline{\rho}/\rho_l)$, identification of volume fractions in the Wigner–Seitz sphere yields the mean pore radius $R(t)$ from the equivalent relationships

$$\frac{4\pi}{3}R^3 N = 1 - (\overline{\rho}/\rho_l) = 1 - (t_0/t)^d, \tag{8a}$$

$$\frac{4\pi}{3}R^3 N_0 = (\rho_l/\overline{\rho}) - 1 = (t/t_0)^d - 1. \tag{8b}$$

Combining (8) and (7) yields the aspect ratio of the equivalent mean spherical shell

$$(R/\ell)^3 = 1 - (\overline{\rho}/\rho_l) = 1 - (t_0/t)^d. \tag{9}$$

Equations (8) to (9) hold even if, due to collapse and merger, (6) may not.

2.3. Kinetic and surface energies, Weber number

Under expansion, the kinetic and surface energies evolve and the overall behavior of the system is characterized by their ratio: the Weber number. Because the fluid is assumed incompressible and inviscid, these two energies fully control the system and only two regimes are expected: all situations can be collapsed according to the Weber number alone. The energies can be estimated within the framework of the mean spherical pore of Section 2.2.

The surface energy of a single mean pore is given by the surface tension coefficient σ

$$E_s = 4\pi R^2 \sigma. \tag{10}$$

The kinetic energy is obtained by assuming the velocity field to be radial and divergence free around the mean pore, with a vanishing mass flux at the Wigner–Seitz boundary

$$E_k = \int_R^\ell \tfrac{1}{2}\rho_l \mathring{\ell}^2 \left(\frac{\ell}{r}\right)^4 4\pi r^2 \,\mathrm{d}\, r = 2\pi\rho_l \left(\frac{d/3}{t}\right)^2 \ell^6 \left(\frac{1}{R} - \frac{1}{\ell}\right), \tag{11}$$

where $\mathring{\ell}$ is the time derivative of ℓ which according to (7) and (6) verifies $\mathring{\ell}/\ell = (d/3)/t$. Using identities (6) to (9) we can now represent both mean radius R and Wigner-Seitz radius ℓ only in terms of t and state of the system at t_0. Namely, from (6) we have

$$N_0 \left(\frac{t_0}{t}\right)^d = \frac{3}{4\pi\ell^3}, \tag{12}$$

thus ℓ can be expressed as:

$$l = \sqrt[3]{\frac{3}{4\pi N_0 \left(\frac{t_0}{t}\right)^d}}. \tag{13}$$

Using the aspect ratio (8) we find that

$$R = \ell\sqrt[3]{1 - \left(\frac{t_0}{t}\right)^d}. \tag{14}$$

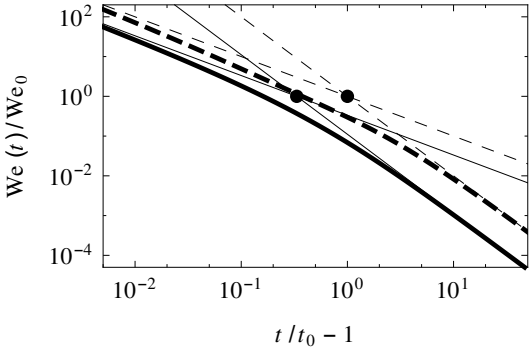

Figure 3: Evolution of the reduced Weber number of the characteristic mean pore during expansion We(t)/We$_0$ in (15a) as a function of reduced time $t/t_0 - 1$ (log scales); solid lines: uniaxial expansion; dashed lines: isotropic expansion; thin lines: asymptotic limits with slopes -1 and -2. Points represent transitions between asymptotic behaviors at small and large times where We/We$_0 = 1$.

Subsequently, we substitute both (13) and (14) in (11), so the Weber number We $= E_k/E_s$ is eventually obtained as

$$\mathrm{We}(t) = \mathrm{We}_0 \frac{d^2\,(t_0/t)^{2-d}}{3\,(1-(t_0/t)^d)}\left(1 - \sqrt[3]{1-(t_0/t)^d}\right), \tag{15a}$$

$$\mathrm{We}_0 = \frac{\rho_l}{8\pi\sigma N_0 t_0^2}. \tag{15b}$$

Notice here that the Weber scaling We$_0$ built from quantities at $t = t_0$ is *not* equal to We(t_0): it is actually found that We$(t) =$ We$_0$ at $t/t_0 \approx 1.16$ and 1.38 for respectively $d = 1$ and 3—with volume expansion ratios of $\rho_l/\overline{\rho} = (t/t_0)^d \approx 1.16$ and 2.60. As illustrated in Fig. 3, the Weber number We(t) diverges as $(t - t_0)^{-1}$ for $t \to t_0$ and vanishes as $(t - t_0)^{-2}$ for $t \to \infty$. The expressions in (15) were scaled in such a way that these asymptotes actually intersect at We$_0$ for either $t/t_0 = 4/3$ or 2 for uniaxial and isotropic expansions as shown in Fig. 3.

The fact that the Weber number We(t) decreases from virtually unbounded values down to zero shows that two regimes should appear during expansion. Kinetic energy dominates at early times and expansion is quasi-ballistic, whereas later, surface tension dominates, thus slowing expansion and inducing pore interactions through Laplace pressure. The transition will appear more or less early depending on the initial conditions defined by the Weber scaling We$_0$ and possibly in either of the $t \to t_0$ or $(t - t_0)^{-2}$ regimes represented in Fig. 3. According to the N_0 dependence in (15b), these two regimes correspond to respectively dense or sparse distributions of cavitation nuclei.

2.4. Pressure Evolution

Mean macroscopic p evolution has been sketched in Figure 1, presenting its sharp drop after the shock and during accelerated expansion phase. At the moment of pore opening pressure changes sign, while its growth is restored in the micro-spall regime. We can trace this evolution in a more detailed manner using velocity potential $\phi(t)$ and mean radii R. We first formulate the Bernoulli equation

$$\phi_t + \frac{u^2}{2} + \frac{p - p_\infty}{\rho} = 0, \tag{16}$$

where $u = \dot{R}R^2/r^2$ and thus $\phi = -\dot{R}R^2/r$. This leads to a Rayleigh-Plesset type expression for pressure "at infinity"

$$p_\infty = -\rho_l\left(\ddot{R}R + \frac{3}{2}\dot{R}^2\right) - \frac{2\sigma}{R}. \tag{17}$$

Having discussed the mean spherical cell aspect ratio in the previous subsection, we can now solve for $\ddot{R}$ using (8) leading to

$$\ddot{R} = -\frac{2l_0}{9\sqrt[3]{t}}\,(t-t_0)^{-5/3}\,, \tag{18}$$

which allows us to retrieve p_∞ by substituting back to (17):

$$p_\infty(t) = \frac{\rho_l l_0^2}{18\sqrt[3]{t_0^2(t-t_0)^4}} - \frac{2\sigma}{\rho_l}\sqrt[3]{\frac{t_0}{t-t_0}}. \tag{19}$$

It is easy to verify that the above formula depicts a curve whose shape corresponds closely to the pressure curve sketched in Figure 1 as long as $t_0 \ll l_0$. The latter is normally the case since mean Wigner-Seitz radii will be significant at the moment of pore opening.

While the simulations described in this work are set up in such a way that initial time value is $t_1 > t_0$, it is interesting to study the effect of the propagating pressure pulse on the system. This reasoning is not without substance, as in computational practice the flow will respond to imposed expansion boundary conditions used here with a negative pressure pulse (see e.g. Figure 7 in (Malan et al., 2018) and results presented in Section 5). We assume incompressibility, however because of the negative pressure created by surface tension on the bubbles/pores, the system could be seen as having negative compressibility, so that the speed of sound c, given below:

$$c^2 = \frac{\partial p}{\partial \rho} \tag{20}$$

is imaginary. Taking this into account, and linearizing the Euler equation (5) and the mass conservation equation (3) we obtain

$$|c|^2\partial^2_{xx}p + \partial^2_{tt}p = 0 \tag{21}$$

A quick estimate based on Laplace's law leads to

$$|c|^2 = \frac{\sigma}{4\pi N\rho_l R^4}. \tag{22}$$

A conclusion that may be drawn from the pressure equation (21) is that as soon as the pressure has been affected by growing pores in a region, the pressure pulse will propagate to the rest of the system at a speed $|c|$. Such a propagating solution, of the form $p = \mathrm{atan}(x/|c|t)$, is possible even in the elliptic system case. The speed $|c|$ of the wave may be comparable to the initial speed $L_0/(2t_1)$ of the expansion wave; comparison will be dependent on surface tension and Weber number.

3. Computational Methods

3.1. The PARIS-Simulator

The simulations presented in this paper use the Parallel Robust Interface Simulator (PARIS-Simulator Ling et al., 2015; Malan et al., 2018; Salvador et al., 2018), which is an in-home CFD code developed jointly at Institute ∂'Alembert, University of Notre-Dame and University of Bologna. PARIS-Simulator is a classical, MAC-type solver using uniform, cuboidal meshes. The strengths of the code lie in a very efficient MPI parallelisation and broad variety of implemented computational methods, especially for interfacial, two-phase flows. These include e.g. Front Tracking[1] (Tryggvason et al., 2011), Volume of Fluid (Hirth and Nichols, 1981) and tracking Lagrangian particles. The code is GPL licensed[2] and publicly available[3].

A well known projection scheme (Tryggvason et al., 2011) is used to solve momentum conservation equations. We will explain it briefly by showing a way the algorithm progresses from n-th to $n+1$-st step. Knowing the values of all fields at the end of $n-$th step, we are starting with the definition of the temporary velocity field $\mathbf{u}^*$

$$\frac{\mathbf{u}^* - \mathbf{u}^n}{\Delta t} = -\mathbf{u}^n \cdot \boldsymbol{\nabla}_h \mathbf{u}^n. \tag{23}$$

It can be found easily since, at the end of n-th time-step it is the only unknown in above formula. The symbol $\boldsymbol{\nabla}_h$ stands for the discrete differential operator. This is a *projection* step, since velocity is projected onto a space with zero pressure field. We can now write a discrete version of (5), which involves $\mathbf{u}^*$, only this time changing the way the approximation of temporal derivative is formulated

$$\frac{\mathbf{u}^{n+1} - \mathbf{u}^*}{\Delta t} = -\frac{\boldsymbol{\nabla}_h p^{n+1} + \sigma\kappa\mathbf{n}\delta_s}{\rho^n}, \tag{24}$$

where superscript $n+1$ stands for the value at the end of n-th time-step. Notice surface tension contribution has been included in (24): σ stands for the surface tension coefficient, $\mathbf{n}$ is the vector normal to the interface, while κ is scalar curvature—also the restriction to the interfacial surface S is ensured by the δ_S operator. If now we apply a divergence operator to both sides of (24) and remember that we assume $\boldsymbol{\nabla}\cdot\mathbf{u}^{n+1}$ to vanish, we obtain the Poisson equation from which pressure p^{n+1} can be found

$$\boldsymbol{\nabla}_h \cdot \left[\frac{\Delta t}{\rho^n}\boldsymbol{\nabla}_h p^{n+1}\right] = \boldsymbol{\nabla}_h \cdot \mathbf{u}^* + \boldsymbol{\nabla}_h \cdot \left(\frac{\Delta t}{\rho^n}\sigma\kappa\mathbf{n}\delta_s\right). \tag{25}$$

In most computational codes numerical solution of (25) is the stage to which most computational cost (up to 90 percent) is associated; especially in multi-phase flows with variable density. Once (25) is solved and p^{n+1} found, both it and $\mathbf{u}^*$ are used to find the divergence-free velocity at the end of the time-step

$$\mathbf{u}^{n+1} = \mathbf{u}^* - \frac{\Delta t}{\rho_n}\left(\boldsymbol{\nabla}_h p^{n+1} + \sigma\kappa\mathbf{n}\delta_s\right) \tag{26}$$

[1] Not used in this work.
[2] https://www.gnu.org/licenses/gpl.html
[3] Available at http://www.lmm.jussieu.fr/~zaleski/paris/index.html

thus ending the procedure. Many authors call (26) a "correction" step as solenoidal character of $\mathbf{u}^{n+1}$ is ensured thereby.

3.2. Interface Tracking

As mentioned, the normal vectors $\mathbf{n}$ and the curvatures κ in above equations[4] are found from the color/fraction function C, whose advection equation follows in discrete form

$$\frac{C^{n+1} - C_n}{\Delta t} + \boldsymbol{\nabla}_h \cdot (C\mathbf{u}^n) = 0. \tag{27}$$

Equation (27) cannot be solved directly, as C is a sharp jump function: the jump would be diffused by numerical errors (Youngs, 1984). Therefore, in most applications (27) is solved using specially crafted geometrical reconstruction–advection schemes such as CIAM (Li, 1995) or PLIC (Aniszewski et al., 2014). Normal vectors and curvature are calculated using Height Functions technique (Cummins et al., 2004; Popinet, 2003), which has multiple provisions for the cases of insufficient grid resolutions and/or specific interface configurations. In the PLIC (Piecewise Linear Interface Calculation (Tryggvason et al., 2011)) scheme, the fluxes $C\mathbf{u}$ are calculated geometrically as intersection volumes between cubic grid-cells and planes, the latter representing the interface. Interface is represented in planar form which is done by first retrieving the vector $\mathbf{n}$ normal to the interface (oriented along the ∇C); allowing us to the interface equation:

$$\mathbf{n}\mathbf{x} = \alpha, \tag{28}$$

where the α term (shift along the normal vector) has yet to be found. Since, however, for each cell the fraction function value C_{ijk} is known at the beginning of the timestep, we want the interface representation to be consistent with it, in other words the volume V_{ijk} of fluid contained on one side of the interface has to be consistent with the fraction function value. However,

$$V_{ijk} = V_{ijk}(\alpha) = C_{ijk} \tag{29}$$

which is solved allowing α to be found. Equation (29) can be solved analytically even in three dimensions (Scardovelli and Zaleski, 2000; Aniszewski, 2011) however, approximate solutions have been published as well (e.g. Newton-Rhapson used in (Ménard et al., 2007)). Moreover, various "simplified" versions of geometric Volume of Fluid method exist that either use an "incomplete" interface representation (e.g. without the α term (Marek et al., 2008)) or don't employ planar representation at all (Xiao et al., 2011). In our implementation of PLIC/CIAM, once the full planar interface reconstruction is finished and (28) is known, the cube-chopping algorithm (Scardovelli and Zaleski, 2000; Tryggvason et al., 2011) is used to find fluxes $C\mathbf{u}$ and enable solution of (27). In our implementation, fluxes are found in a "split" manner, e.g. along each of the axes separately – the order being permuted at each solver iteration (Pilliod and Puckett, 2004).

[4]The same applies for the approximation of Dirac delta δ_s.

More details about the interface tracking and advection methods used here can be found e.g. in comparative work (Aniszewski et al., 2014), comprehensive textbook (Tryggvason et al., 2011) or, in context of PARIS-Simulator (Ling et al., 2015; Salvador et al., 2018).

3.3. Free Surface Solver

To implement the boundary conditions on the interface, a free surface method has been programmed in PARIS-Simulator (Malan and Zaleski, 2015). The flow within the pores is not explicitly solved for (except up to two interior cell layers as explained below), additionally in this paper we initially set the p_p pressure value to zero. With that assumption, the flow is in fact a quasi-single phase flow, but surface tension is accounted for on the pore surfaces. Still, in this case the pressure p_p inside the pores is defined, although it is assumed spatially constant inside them and is calculated using the polytropic equation of state (Malan et al., 2018).

1. The pressure field is extrapolated onto the interface which is necessary for (25). The boundary value of the gradient is computed as
$$p^* = p_p - \sigma\kappa, \tag{30}$$
where p_p is constant pore pressure, and $\sigma\kappa$ is Laplace pressure, thereby assuring that surface tension effect is accounted for. The p^* value is used for $\boldsymbol{\nabla}_h$ operators in cells neighboring the interface;
2. The velocity field is extrapolated to within the pores; these values are necessary for higher-order gradient operators for cells neighboring the interface. Extrapolation is based on liquid velocity, which is extended to two grid-cell layers (or 'levels') within pore/bubble interior by geometrical fitting and least-squares minimization;
3. Finally, the extrapolated velocities in level 1 and 2 cells are corrected to ensure the new field is divergence free.

Computational tests have shown that the above procedure amounts to approximately 10% of CPU cost in a massively parallel simulation compared with Poisson solver cost standing at 80%.

A limitation introduced by current implementation of the above algorithm is—apart from aforementioned necessity of pre-seeding the pores—that the voids cannot coalesce, as it is not yet made compatible with the point 2 above (velocity extrapolation to within the pores). of the above list, as topology change of the pores cannot be accounted for. The model however allows for the pore collapse, to which the system responds with a pressure pulse. It is also interesting to notice that the pores can undergo displacement (i.e. move) for example due to non-balanced surface tension force distributions. More details on the Free Surface sub-solver implementation can be found in Malan et al. (2018).

3.4. Implementation

In implementation, we apply the Hypre package's (Falgout and Yang, 2002) SMG (semi-coarsening multigrid solver with 3D plane smoothing) for numerical solution of the Poisson

problems (25) on the structured, cubic meshes. Advection terms in (23) are calculated using central differencing with WENO (Shu, 1997) and Superbee-type (Sweby, 1984) slope limiters. A cavity tagging and Lagrangian particle-tracking algorithm (Ling et al., 2015) are used to retrieve statistics of cavity sizes. Interface curvatures for (24) are calculated with a combination of techniques providing for various stencil shapes and built within the framework of Height Function method (Cummins et al., 2004) and with the mixed-Youngs-central (Youngs, 1984) scheme for normal vector $\mathbf{n}$ computation. Temporal discretization is performed using the second-order Crank-Nicholson scheme (Carnahan et al., 1969); the code can also be switched to first order Euler scheme for testing purposes.

The method was validated comparing numerical solutions to solutions of the Rayleigh–Plesset equation for oscillating bubbles (Malan and Zaleski, 2015; Malan et al., 2018, Fig. 5 in the latter). In the test, a perfect match was found between the Rayleigh-Plesset prediction for the cavity volume temporal evolution and a computed volume, proving that the chosen combinations of computational methods neither adds nor looses traced volume. Additional test is provided in section 3.5

3.5. Free Surface Advection Test: 2D Expanding Cavity

Here, we briefly present a simulation set up to test the accuracy of the VOF-PLIC advection scheme coupled with the Free Surface solver (as described in Sect. 3.3). Unlike synthetic advection tests performed traditionally in context of VOF using passive velocity fields – such as circle/sphere advections (Aniszewski et al., 2014) – the "expanding cavity" test case involves solution of the Euler equation (5) i.e. $\mathbf{u}$ and p are solved for at each iteration. In this sense, it resembles the high-density droplet advection presented by Vaudor et al. (Vaudor et al., 2017) which also solves for all terms of Navier-Stokes equations in a flow with simple initial conditions and a trivial analytic solution . Here, too, any errors in the advection procedure or Free Surface coupling would manifest itself.

The premise of the test is simple. A two-dimensional, square domain of size 1 is defined as filled with 'liquid' of density $\rho_l = 1$, with a single circular pore (cavity) initialized in the center. Isotropic expansion is imposed by setting a constant normal outflow velocity $\mathbf{u}_n$ such that $\forall t\colon \mathbf{u}_n(t) = 0.05$. This way liquid flux through each of the walls is equal to $q = 0.05{\times}1$, thus the rate of cavity volume (surface) growth must be described by:

$$R_c(t) = \pi r_0^2 + 0.05 \cdot 4t, \tag{31}$$

where $R_C(t)$ is the cavity surface at time t, and r_0 stands for initial cavity radius. In the simulation, by convention the grid cells with $C_{ij} = 1$ signify the cavity interior, while those with $C_{ij} = 0$ are in the liquid (intermediary values $0 < C_{ij} < 1$ represent interface cells). Thus, total sum of fraction function may be used to represent the computed cavity surface $V_c(t)$ at any time:

$$V_c(t) = \sum_{i,j}^{N} C_{ij}(t) \cdot (\Delta x)^2\,, \tag{32}$$

where N is the number of grid points in each direction, and Δx is grid-cell size. Combining (31) and (32) yields a definition of the L_1 advection error as a function of time:

$$L_1(t) = |\pi r_0^2 + 0.05 \cdot 4t - \sum_{i,j}^{N} C_{ij}(t) \cdot (\Delta x)^2\,|. \tag{33}$$

For the test, a relatively large value of initial cavity radius was chosen at $r_0 = 0.2$, to ensure that the pore is properly resolved at 16^2 grid (3 grid-cells in radius). Cavity was expanded over $2.5 \cdot 10^4$ time-steps fixed at $dt = 1 \cdot 10^{-4}$ resulting in $t_{end} = 2.5$, and final radius of $r_{end} = 0.45$. Surface tension was set to zero.

Table 1: Reconstruction error of the circular pore E_r at varying grid levels.

Grid points	E_r	Ratio	Order
16^2	$2.97 \cdot 10^{-5}$	–	–
32^2	$8.29 \cdot 10^{-6}$	3.59	1.79
64^2	$1.99 \cdot 10^{-6}$	4.16	2.08
128^2	$4.93 \cdot 10^{-7}$	4.03	2.01

We have investigated the error inherent in initial PLIC representation of the circle at each grid resolution – caused by the fact that the interface is represented by linear segments. This reconstruction error (noted E_r) is easily calculated as difference between πr_0^2 and $V_c(0)$. It is summarized in Table 1. We can see that second order convergence of the interface reconstruction scheme is obtained, as expected for PLIC type method (see for instance López et al., 2005, Table 1). Representation errors have been accounted for in the final test result.

Table 2: Final L_1 error values for expanding cavity test at varying grid levels.

Grid points	$L_1(t_{end})(\times 10^{-5})$	Ratio	Order
16^2	7.59	–	–
32^2	4.721	1.608	0.8
64^2	2.801	1.685	0.84
128^2	0.669	4.18	2.09

Final $L_1(t_{end})$ values are presented in Table 2. Proper convergence is observed at order roughly one, which only improves when the finest grid is used. This is consistent with order of the procedure we have chosen in this test to perform extrapolation of $\mathbf{u}$ to within the pores (see also Malan et al., 2018, Sect 3.3 therein) and with first order Euler discretization in time used in this test[5]. Although not shown here, we have repeated the test in three dimensions finding a similar convergence. We thus conclude the method properly conserves tracked cavity volume, as the latter remains in good agreement with analytic prediction. Having confirmed the volume tracking capability of our coupled Free Surface-VOF code, we now focus our attention on its application in context of micro-spallation.

[5] Other results presented in the paper employ the Crank-Nicholson scheme.

4. Micro-spall simulation setup

4.1. Initial Conditions

To simulate the idealized micro-spall phenomena specified in Section 2, we have set up the simulations as follows. Cubical computational domain is used (see Fig. 2), containing a given number of pre-seeded pores in a FCC (Face-Centered Cubic) lattice. It is "expanded" in x direction as assumed in Section 2. More specifically, the proper temporal evolution of the velocity field described by (1) is ensured by initializing:

- the x-velocity component to $u = x$ with proper translation and scaling, so that for $t = t_1$ we have $u(0, t_1) = -u_n$, $u(L/2, t_1) = 0$ and $u(L, t_1) = u_n$ where u_n is the outflow velocity;
- the outflow boundary condition for the velocity field $\mathbf{u} = (u, v, w)$ in such manner, that

$$u_n = 1/t_1, \tag{34}$$

  where $t_1 > 0$; for subsequent moments of simulated time t (34) is held so that $|u_n(t)| = 1/t$ at all times;
- the v and w components equal to zero.

This implies usage of Dirichlet boundary condition for u in the x direction, which is time-dependent as was said above. Neumann boundary condition for p is thus applied on the $x+$ and $x-$ walls. Imposing Dirichlet boundary conditions for pressure – instead of for velocity – could be a valid choice for this type of flow, however – unlike the cases in which pores are wholly contained in the domain (Malan et al., 2018) – uni-axial expansions discussed here involve pores crossing outer domains along x axis. This in turn would make Dirichlet condition for pressure inconsistent.

Periodic boundary conditions are imposed on YZ walls. For the condition to be compatible with the pore cluster geometry, it is re-shaped by adjusting the pore-free buffer surrounding it. More precisely, due to periodic condition in YZ directions, the buffer is present only in the x direction (visible as empty region in Fig. 2), i.e. for $x < 0.12$ and $x > 0.88$ the domain contains no pores at $t = t_1$. Cubic domain of size $L = 1$ is assumed with 365 pores. Thus, we arrive at $\ell \approx 0.14$.

4.2. Physical parameters and computational grids

We describe simulation results concerning the uniaxial expansion using example simulations whose parameters are given in Table 3.

Consider now the simulation domain $(-L_0/2, L_0/2)^3$ within which spherical pores are initialized with non-zero radii (which is necessary due to limitations of PARIS-Simulator code) i.e. numerical simulations are started at $t_1 > t_0$. With this in mind, the mean radii distribution right after pore opening is

$$R(t_1) = L_0 \left[\frac{3}{4\pi N_0} \left(\frac{t_1}{t_0} - 1 \right) \right]^{1/3}, \tag{35}$$

which is how pores are defined in the initial simulation condition. In this computational configuration, it is desirable for $R(t_1)$ to be possibly small, in order to offer a large range of scales - in other words, headroom for $V(t)$ growth before the pores coalesce. A favourable relation would be

$$\Delta x \ll R(t_1) \ll \ell \ll L_0, \tag{36}$$

where Δx is the grid size. The leftmost and rightmost inequalities of (36) are however slightly relaxed for the results presented in this paper due to grid resolutions used, as will be detailed below.

Example simulations have been performed using 256^3 grid points. For the first simulation ("I"), value of Weber number (15a) at t_1 is 512.83. The pore lattice is configured as specified above, with liquid characteristics found in Table 3. In the Table, "I" and "C" are labels designating the "Isolation" and "Competition" regimes; We and Ma are dimensionless Weber and Mach numbers, ρ and σ are respectively liquid density and surface tension applied at the pore surfaces, while var(r) stands for the variation in pore radii applied to the initial condition. Mach number values presented in Table 3, are calculated using the speed of sound c as defined by (22).

As mentioned above (see (35)), due to the applied spatial resolution, certain restrictions on the initial pore radii $R(t_1)$ are imposed since the pores must be properly represented by the interface tracking method at t_1 . This representation requires e.g. that gradients of the fraction function C can be resolved near the interface (to calculate interface normals) with finite difference operators. Having the size of domain L_0 and initial pore number N_0 fixed, and imposing additional restriction $R > 3\Delta x$ we e.g. choose $t_1 = 0.08$ for the presented simulation of isolation regime (see Table 3). This amounts to $R(t_1)/\Delta x \approx 3.44$ which is considered resolved (Tryggvason et al., 2011) in that proper values of curvature can be computed for pores of that radius[6]. Due to the dependence (8) between simulation initial time t_1 and bubble/pore radii, any decrease of t_0, and t_1/t_0 would reduce R, which in turn would imply an increased grid resolution.

5. Results

5.1. Isolation regime

Figure 4a presents cluster geometry at $t' = t_1 + 1.929 \cdot 10^{-2}$. Uniform expansion of the bubbles/pores is clearly visible with pore layers closest to the walls along the x axis visibly elongated due to the fact that convection is strongest there. At $t \geq t_1 + 1.92 \cdot 10^{-2}$ one observes pore radii of order ℓ. Nearly all pores are ellipsoidal in shape, and have expanded beyond the region of the simulated volume, including periodic yz walls. Moreover, the outer layer of pores has now completely disappeared (have been convected out) from the simulation domain, and only remnant interfacial cells are visible.

Temporal evolution of the pore volume fraction V_g for "I" regime flow is seen in Fig. 5. Seeing as all volume change in the liquid results from growth of the pores, we can supplement (4) by a following expression for pore volumes:

[6] Not accounting for about 5 percent variance in R in initialization.

Table 3: Parameters for two examples of simulations of the uniaxial expansion, as explained in text.

Label	ρ	σ	t_1	t_0	var (r)	We(t_1)	Ma(t_1)
I	1000	0.1	$8 \cdot 10^{-2}$	$7.797 \cdot 10^{-2}$	50%	512.83	15
C	444	1	2.1	2.092	50%	$3.3 \cdot 10^{-2}$	0.12

$$V_g = L_0^3(1 - \frac{t_0}{t}). \tag{37}$$

The initial pore volume fraction at t_1, i.e. $V_g(t_1 = 0.08)$ should amount to $3.59 \cdot 10^{-3}$, however it is slightly higher at simulation init, due to the initial variance in pore radii (Table 3). Proper scaling has thus been used for the analytic formula (37) to make up for that in Fig. 5.

Generally, one observes a difference between analytic prediction and simulated pore value in Figure 5. In our opinion, there are two main reasons for that. One is –as mentioned in context of Fig. 4a – that the pores leave the computational domain while it is expanded, which in the "I" simulation takes place at $t + t_1 > 0.05$ so very near to the beginning of the x range (this moment is marked in Fig. 5 as t_{ex}). Naturally, this means that vacuum volume (areas with $C = 1$) associated with these pores is no longer represented in the sum shown in Fig. 5. Moreover, once the pores are sufficiently large the case is no longer dilute, thus departing from the model assumptions as the $R(t) \ll \ell$ requirement of (36) doesn't hold, also the pores are no longer spherical.

For the isolation regime simulation, we additionally present in Fig. 6 the profiles for $\langle p \rangle$ (Fig. 6a) and $\langle u_x \rangle$ (Fig. 6b) measured along the x axis. These are taken from the early simulation stage ($t = t_0 + 6.732 \cdot 10^{-3}$) and confirm that the evolution of the system is indeed in the ballistic regime, while the velocity profile conforms to linear as predicted in (1). The 'wavy' character of the plot in Fig. 6b, is caused by inclusion of zero velocities (inside the pores) to the average. Similarly, we observe no variance in $\langle p \rangle$ (Fig. 6a) when focusing our attention on the lattice-occupied part: for $x < 0.12$ and $x > 0.88$ there is an empty "buffer zone" in the x direction, as mentioned above.

5.2. *Competition regime*

We continue the description of the results with the second simulation ("C") which, as seen in Table 3 is characterized by a much lower Weber number. As a result of this, the evolution of the pore lattice is no more dominated by expansion and the pores are not isolated, and the elongated shapes of the pores visible in Fig. 4a give way to a "pore competition" phenomenon (Everitt et al., 2006). Figure 4b, shows that number of pores has either shrunk or is at the verge of imploding, their volume being overtaken by a group of large pores. Distribution of radii in the latter group is rather isotropic, with all pores roughly spherical, while ellipsoidal forms are absent. For situation presented in Fig. 4b average pressure $\langle p \rangle$ has a negative value. This is due to the fact that positive pressure field is associated with expanding liquid, while for low Weber number negative Laplace pressures (capillary force) dominate the pressure distribution. We will revisit this subject in Fig. 10.

A comparison between (37) and calculated pore volume (analogous to Figure 5) is presented for the "competition" regime in Figure 7. For this low Weber number case, we note a virtually perfect fit of calculated total pore volume (obtained using a sum of fraction function C) up until $t_{ex} = 0.133$ which is the moment at which first pores exit the calculation domain. The overall better fit might be due to the fact that in the absence of dominating uni-axial expansion, the pores remain generally spherical, as assumed in Sect. 2. It is interesting to note that in this case $V_g(t)$ minimally surpasses predicted values just after t_{ex}, before visibly dropping below it for $t - t_1 > 0.25$. Initial slight increase in $V_g(t)$ might be due e.g. to interaction with periodic walls, which the pore cluster contacts first. The subsequent decrease in $V_g(t)$ is coincident with first pore implosions and should be associated with them.

It is worth noting both Figures 5 and 7 may serve as an additional, indirect evidence of traced mass/volume conservation by our method. This is due to the fact that pore expansion described by (37) is the only source of the increase of the total C function, and a good agreement with it is reached at least as long as pores remain spherical and don't leave the domain.

Increased radii variation and implosion events that characterize the competition regime, are visible in Fig. 8a which displays individual pore volume histories for the larger (maroon lines) and smaller (turquoise lines) Weber numbers. To the accuracy allowed by post-processing software, each line displays volume of an individual pore, with up to 100 of the randomly chosen pores tracked for each simulation. Time is normalized by capillary timescale (Malan et al., 2018)

$$\tau_R = \left(\frac{\rho R^3}{\sigma}\right)^{1/2}, \tag{38}$$

which results (due to parameters presented in Table 3) in factor of 5 between the two simulations presented in Fig. 8a, accounted for in the figure. Unlike the high-We regime, in which expansion is rapid and nearly uniform, the low-We competition regime exhibits higher variance in pore volumes, with a number of implosion events visible towards the end of recorded time. This proves that the presented numerical method is capable of capturing the transition between the two regimes, provided that simulation covers a sufficient temporal range[7]. Additionally in Fig. 8a we observe a sub-population of bubbles exiting the domain through the side-walls towards $\tau_D = 0.05$.

This flow stage is visualized again in Figure 8b which contains a magnification for $\tau_D \in [0.02, 0.05]$. Even at this time

[7] Which in turns depends directly on numerical grid resolution. The smaller $R(t_1)$ the more timespan will be included in the simulation before the pores coalesce.

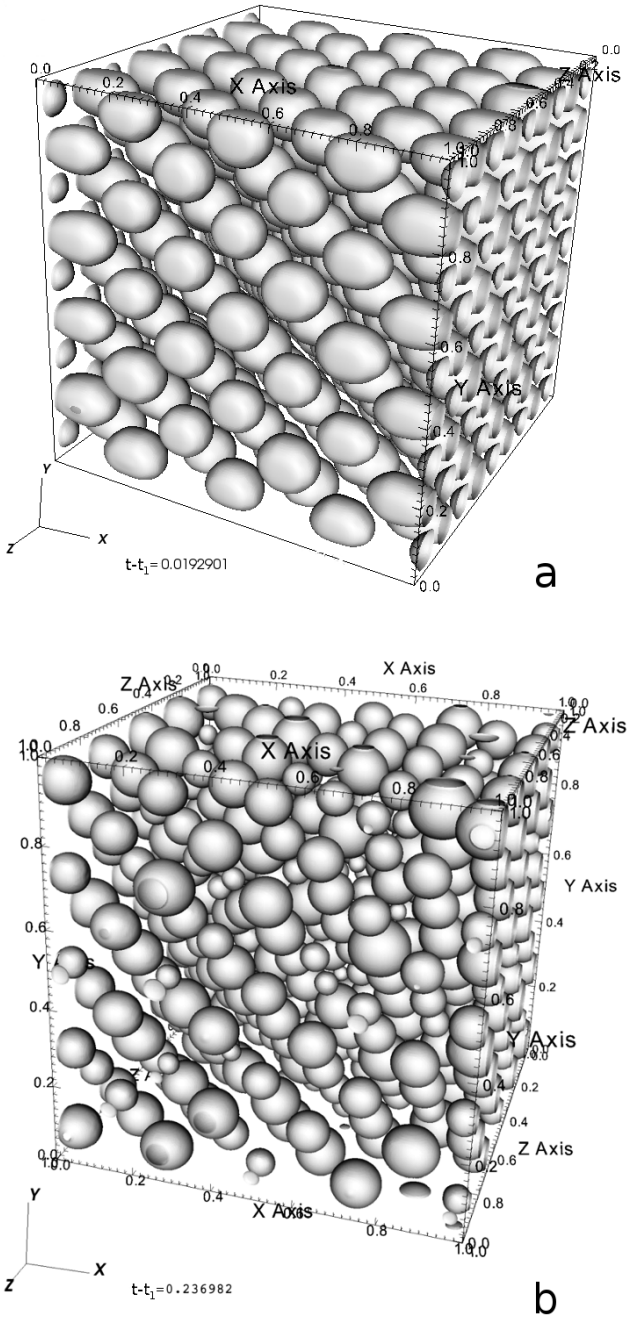

Figure 4: (a) Simulation of the flow characterized by We = 512. (isolation regime) at $t = t_1 + 1.92 \cdot 10^{-2}$. (b) Simulation of the pore lattice at We = $3.3 \cdot 10^{-2}$ ("competition" regime) for $t = t_1 + 0.237$.

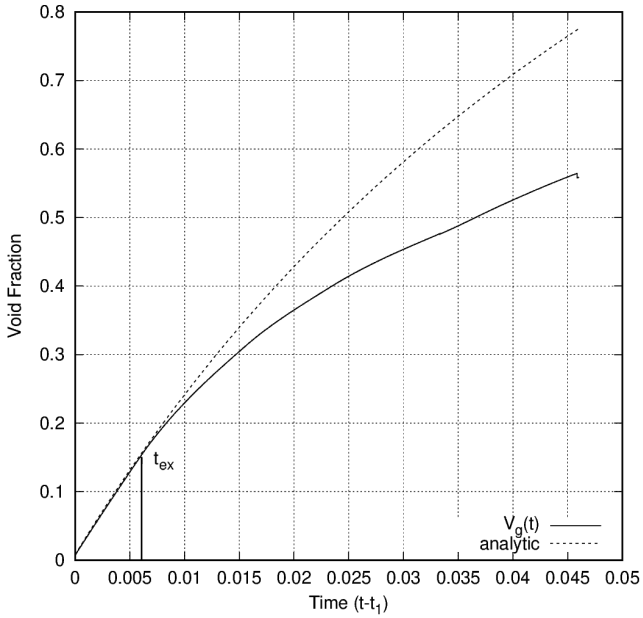

Figure 5: Volume fraction temporal evolution (isolation regime). Continuous line: simulation; dashed line: using (37). The moment at which first pores touch domain boundary is marked with vertical line and the t_{ex} label.

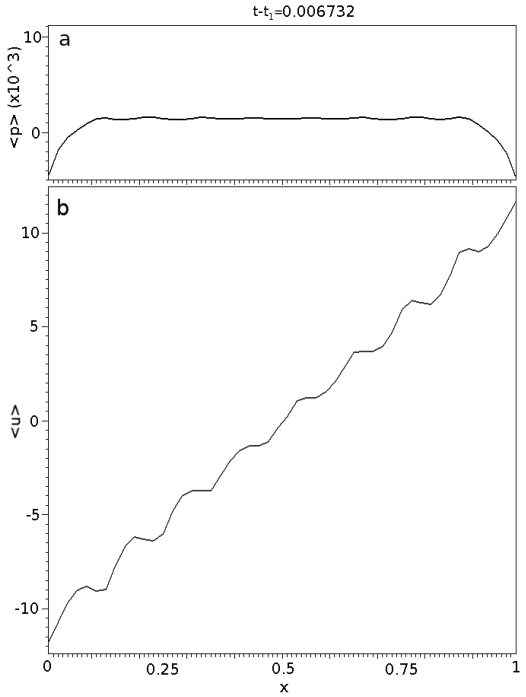

Figure 6: Isolation regime: Averaged (in YZ) profiles of p (a) and u (b) for $t - t_0 \approx 6 \cdot 10^{-3}$. (The x range applies to both sub-plots.)

scale we observe that a distinct group of pores loses volume at identical rate: those lines represent the group of approximately 50 pores that are carried out of the simulation domain. It is a visibly different evolution than that presented by the maroon lines in Fig. 8a. The latter is characterized by individual collapses/implosions taking place for $\tau_D > 5.5$, and absence of distinct pore sub-groups. The same character of volume evolution in the competition regime has previously been reported in (Malan et al., 2018) (see Figure 7 therein, note their plots show all individual pores while Figure 8 presents only population subset). Most importantly, their result – even if obtained for isometric expansions –shows a trend of pore population to create discrete groups characterized by specific growth rates, which is more visible the higher We is. Our result visible in Fig. 8a and 8b presents an extreme case of that trend: for "ballistic" expansion only one group exists at We = 512.

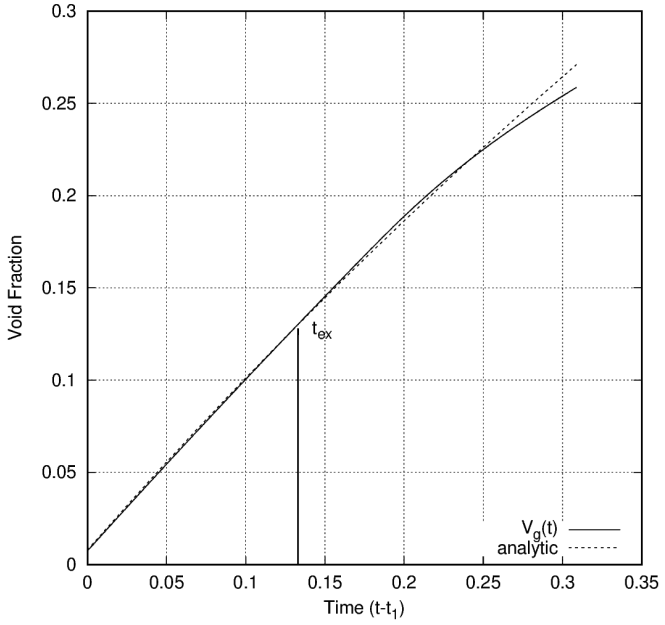

Figure 7: Volume fraction temporal evolution (competition regime). Continuous line: simulation; dashed line: using (37). The moment at which first pores touch domain boundary is marked with vertical line and the t_{ex} label.

Both pore populations visible in Figure 8a reach the coalescence region: for the We = 512 population (maroon) the volumes recorded reach $2 \cdot 10^{-3}$, while for competition regime (turquoise) they are slightly higher at $3.5 \cdot 10^{-3}$. This translates to final equivalent sphere radii of $r \approx 8 \cdot 10^{-2}$ and $r \approx 9.42 \cdot 10^{-2}$ for isolation and competition regimes respectively. Since these radii are in both cases larger than $\ell/2$, coalescence will appear. The probability of pore contact occurring is of course higher in the isolation regime with all pores present. Ultimately, coalescence is the reason why simulation of either regime cannot be continued beyond the τ_D values presented in Figure 8a due to implementation limitations mentioned in Section 3.3.

5.3. *Evolution of the pressure field*

We continue our comparison of the presented uniaxial expansion regimes with Figs 9a and 9b, first of which displays the evolution of averaged pressure field

$$\langle p \rangle = \frac{1}{V} \int_V p dV \tag{39}$$

for both analyzed flow regimes. As the high-We regime is characterized by a more violent decrease in the average pressure in the initial parts of expansion, it was necessary to plot $\langle p \rangle$ in logarithmic scale in Fig. 9a. However due to the function being negative, we instead plot in Fig. 9a the

$$\log(|\langle p \rangle|) \cdot \mathrm{sgn}(\langle p \rangle). \tag{40}$$

It is clearly visible that the rapid decrease from $e^{10} \approx 2.2 \cdot 10^5$ to zero is followed by a period for which $\langle p \rangle < 0$.

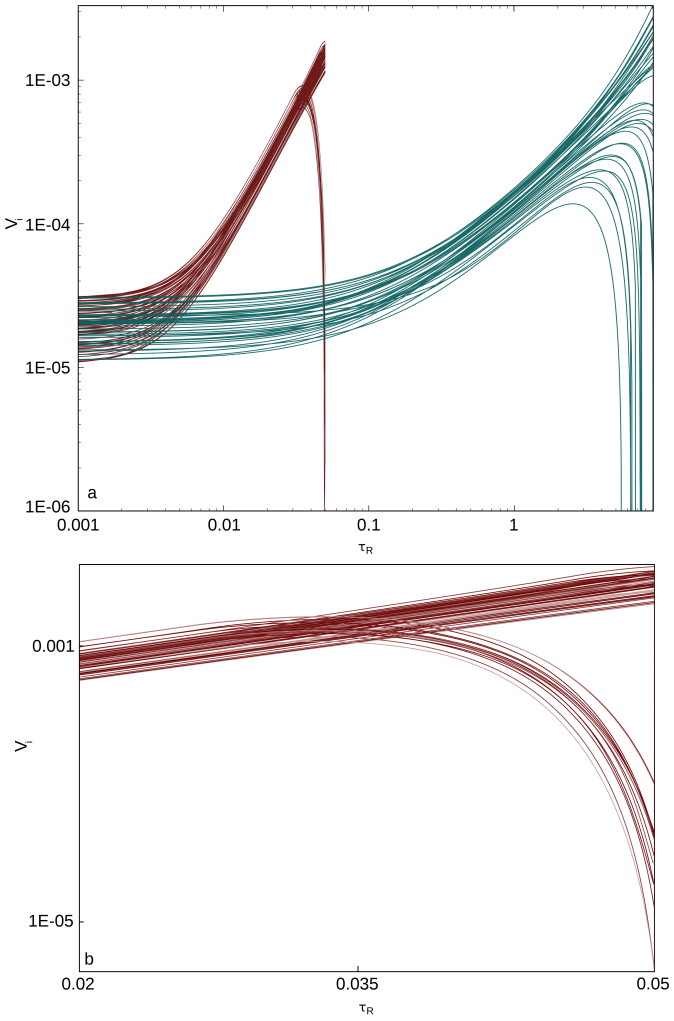

Figure 8: (a): Pores volume history for We = 512 (maroon), and We = 0.03 (turquoise) flows. (b) Enlargement for $\tau_R \in [0.02, 0.05]$, We = 512.

Figure 9b presents a plot comparable to Fig. 9a, but obtained by discarding Laplace pressures (i.e. capillary contributions). Here, we are using only input from grid cells that do not coincide with pore surfaces (this can be found from values of C function)—in other words, grid-cells positioned away from the pores and the interface. This can be roughly approximated by

$$\langle p \rangle = \frac{1}{V} \int_V p(1 - C) dV \tag{41}$$

where C stands for the fraction function (C is associated with pore volume, meaning that a grid cell with $C = 1$ is inside a pore, $C = 0$ corresponds to the liquid, while $0 < C < 1$ signifies an interface cell). Accuracy provided by (41) is moderate, as it will still include contributions from direct neighbours of the interface grid-cells; those neighbouring cells are generally still influenced by Laplace pressures. While better accuracy could be provided by a distance function-based methods (Aniszewski et al., 2014), the above formula is enough to yield a much different result than depicted in Fig. 9a. Indeed, while a similar pressure evolution as in Fig. 9a is observed in Fig. 9b, we notice

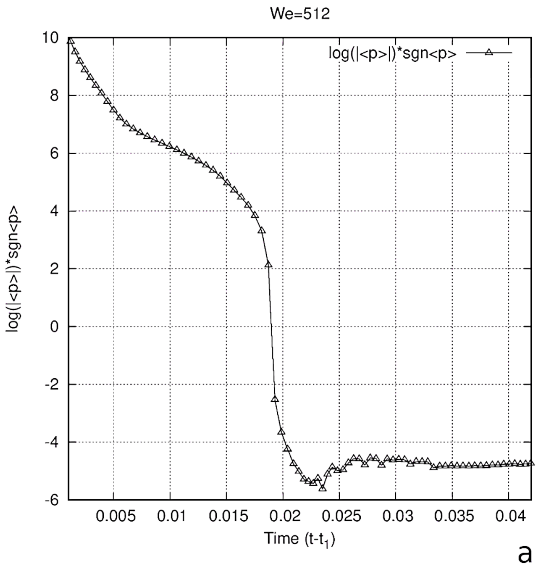

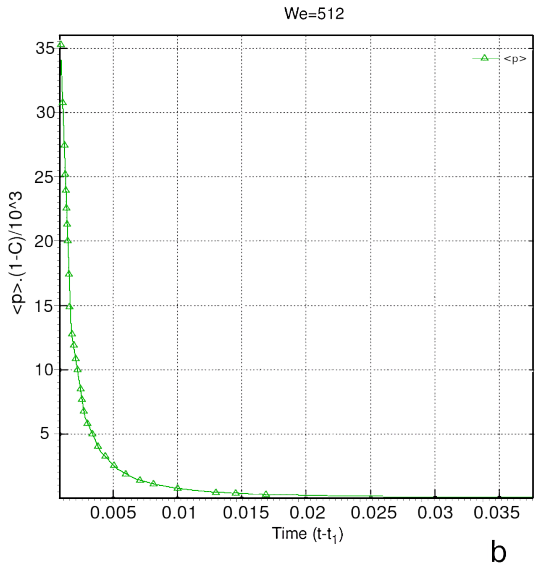

Figure 9: Isolation regime: (a) Evolution of the domain-averaged pressure for the flow at We = 512; (b) The same quantity prepared by including only grid cells in the liquid.

that

$$\forall t\colon \left\{\langle p\rangle(t) > 0 \ \wedge \ \frac{\partial\langle p\rangle}{\partial t} < 0\right\}. \tag{42}$$

This is to say average pressure is always positive and decreasing. Additionally, slight oscillations visible in Fig. 9a for $0.025 < t < 0.035$, are not found in Fig. 9b, thereby reassuring us that they were attributed to the capillary forces.

A different $\langle p\rangle$ evolution is observed for the "competition" regime. In Fig. 10 for low We, which (as we mentioned in context of Fig. 4) is dominated by capillary pressures nearly from the onset, we notice $\langle p\rangle \in [-50, -20]$ within the computed time interval. For $t > 0.15$ the individual peaks are visible (as triangles above other curves in Fig. 10) which should be associated with implosion (collapse) events that result in shocks

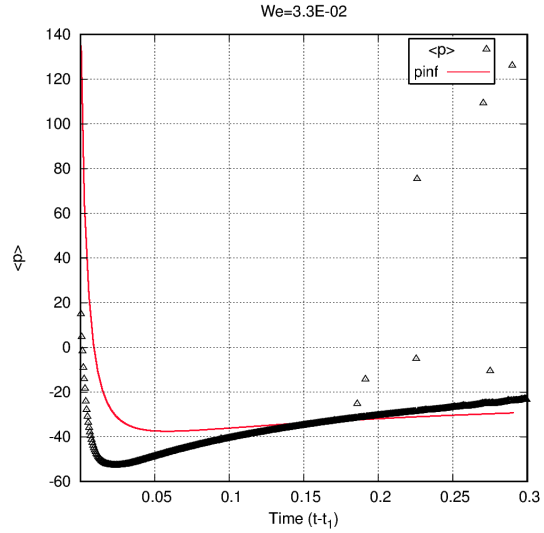

Figure 10: Evolution of the mean pressure field for the competition regime. Numerical simulation (black triangles) and analytical $p_\infty(t)$ using (19) (red line).

to the liquid.

Pore implosions, encountered only in competition regime (low We), are difficult to treat numerically in codes that use uniform grid size cells. Once a pore decreases in size heading into collapse, so does the number of grid-cells coinciding with its surface (i.e. the interface). It eventually becomes so small that interfacial curvature term $\sigma\kappa\mathbf{n}\delta_s$ of (24) can not be reliably calculated. In our implementation (Malan et al., 2018) when encountering this situation PARIS-Simulator removes the vapor cells from the solution, replacing them with liquid cells, supplying a volume sink in form of a source term added to the r-h-s of (25). A consequence of that is a shock wave propagating to the system as described in Section 2.4. This explains pressure peaks visible in Figure 10.

It is easy to note that unlike in the isolation regime, in the competition regime we find for $t > 0.02$

$$\frac{\partial\langle p\rangle}{\partial t} > 0, \tag{43}$$

i.e. average pressure is steadily growing, which in fact is predicted by (19). We would associate this with the initially rapid expansion slowing down, and competition process taking over.

The first expansion phase (or the isolation regime) corresponded to rapid expansion when the pores are still small compared to ℓ, while the latter is due to Laplace (capillary) pressures which—in spite of being inversely proportional to pore radii—become dominant, and competition phenomenon appears (Malan et al., 2018). Note that measured in absolute time values, evolution presented in Fig. 10 involves a temporal interval nearly ten times longer than that of Fig. 9.

To further validate the predictions of the numerical simulation result presented in Figure 10 we have included a curve displaying temporal evolution of $p_\infty(t)$ calculated using (19). The sharp pressure drop resulting from initial shock, as well as the beginning of pressure growth after minimum is reached (mentioned in Section 2), are well visible in Fig. 10 for both curves,

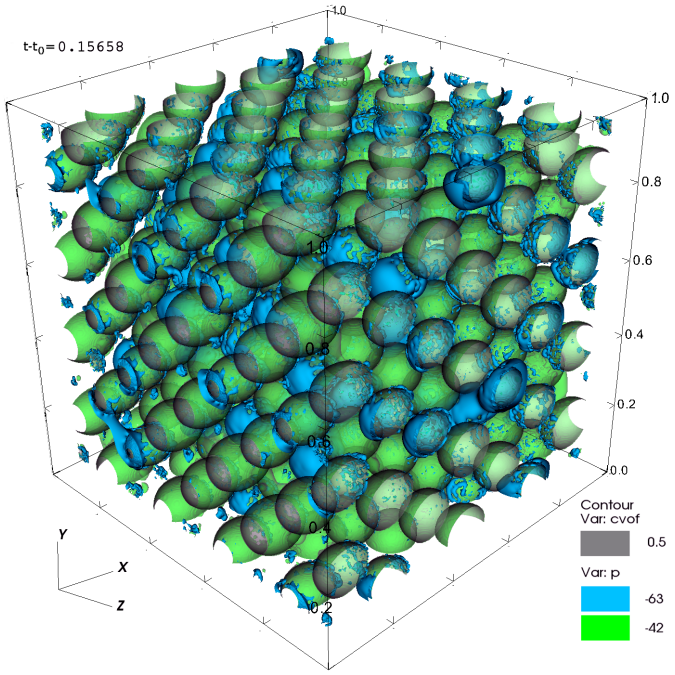

Figure 11: The bubble cluster at We ≈ 0.1, corresponding to a transition from isolation to competition regime.

and there is overall agreement in their shape. Obviously, mean pressure $\langle p \rangle$ is not equal to p_∞ and is strongly influenced by the capillary pressures originating from surface tension on pore surfaces. For this reason, minimum p value is predicted too low. Interestingly, if instead of using $\sigma = 1$ in (19) we calculated p_∞ using $\sigma = 1.3$, we get $\min_t(p_\infty(t)) = \min_t(\langle p \rangle(t))$ and a better agreement of the p_∞ curve to $\langle p \rangle$ overall which strongly suggests that indeed the contributions of Laplace pressures substitute the difference between the analytic prediction and the simulation result.

Figure 11 presents an example of an additional simulation[8] with $\mathrm{We}(t) = 9.56 \cdot 10^{-2}$ at $t = t_0 + 0.157$. This third presented simulation corresponds to a transition from isolation to competition regimes predicted by (15a). We can illustrate this by directing our attention to values of pressure inside the pore cluster. In Fig. 11, three isosurfaces are presented. First, a gray (semi-transparent) isosurface of fraction function C is visible. This marks the position of individual pores, although at first glance it is hard to conclude if the competition phenomenon is present. Similarly, regions with $p \approx -42$ (green, semi-transparent isosurface in Fig. 11) exhibit little spatial variability: all pores are surrounded by them. However, once an isosurface for $p \approx -63$ is drawn (solid blue surface in Fig. 11) we notice that homogeneity is gone close to certain pores' surface. Upon closer inspection it is evident that these pores have smaller radii (hence larger mean curvatures); they are being acted upon by other, growing pores to eventually succumb to the competition (Malan et al., 2018).

[8]The simulation uses the same boundary conditions as those mentioned above, resolution is 512^3 grid points.

6. Conclusions

We have presented a numerical simulation setup that permits prediction of the behavior of a pore lattice within rapidly expanding medium. The expansion corresponds to a uniaxial (one-dimensional) ballistic phenomenon characterized by large initial outward velocity magnitudes which then immediately diminish. On one hand, this setup facilitates recognition of momentum-dominated phenomena such as rapid pore elongation in "isolation" regime. On the other, the decline in expansion rate promotes the onset of pore "competition" and more anisotropic radii distribution in surviving pores. Moreover, simulations allow us to observe transition between these two regimes. We have presented that instantaneous velocity and pressure profiles match analytic predictions, and so does the temporal pressure evolution in the simulated pore systems.

It is relatively easy to point out numerous simplifications of the presented model. One example is the uni-axial mean expansion assumption, another: lack of solution inside pore interiors, yet another is using an incompressible medium. Still, the work presented herein provides us with a rare insight into the micro-spall process at the FCC lattice scale which is otherwise inaccessible experimentally, forcing the researchers to apply modelling and/or indirect analysis. In this context, the present study—especially with its choice of (partly periodic) boundary conditions—may easily be used as a departure point for larger-scale modeling e.g. in the context of metals undergoing spallation under load.

Results presented here can be employed to improve predictions of micro-spallation type damage in an *indirect* manner. Published computations of micro-spall utilize larger domains i.e. simulate larger material samples – up to $180nm$ nickel sample in (Qiu et al., 2017) – over which stress is imposed in similar one-dimensional fashion i.e. [1 0 0] direction of the FCC lattice (consistent with the X axis direction in this work). Individual Ni atoms are presented as Lagrangian particles using the NEMD (NonEquilibrium Molecular Dynamics) approach (Wang et al., 2014), and cavities are created by randomly removing atoms. Meanwhile our simulations include domains orders of magnitude smaller – only a few dozen basic 12-atom FCC clusters versus e.g. $5 \cdot 10^6$ atoms in NEMD (Wang et al., 2014) – but account for some phenomena forcibly neglected at larger scales, such as non-spherical pore shapes and competition.

Thus, assumptions we have taken allow re-using our flow domain as a control volume in a finite volume approach for modelling bigger systems. Slices (of thickness L_0 or $L_0/2$) can be created by repeating the domain in periodic YZ directions. In X, either by using entire domain ($x \in [-L_0/2, L_0/2], u \in [-u_n, u_n]$) or only half ($x \in [0, L_0/2], u \in [0, u_n]$)) one could construct neighbouring slices by using u_n at the right-hand-side of one volume as a condition on the left-hand-side of the neighbouring volume - in this scenario expansion would be uni-directional along X with increasing u_n. Pressure could be treated as locally constant in each control volume (see Fig. 6a). Having thus constructed and analysed the larger system, predictions could be either compared with NEMD-type simulations or used as an initial condition for the latter concerning, for example, initial

vacancy concentration calculated from the $V_g(t)$ evolution presented in this work. This concentration is a critical parameter in spall strength prediction (see e.g. Table 1 in Qiu et al., 2017, and references therein), and, as evident from our results, dependent strongly on the expansion regime.

7. Acknowledgements

Authors acknowledge partial funding from the CEA (Commissariat à l'énergie atomique et aux énergies alternatives); the computations have been partly performed using the CEA's TGCC facility. Visualizations have been performed using *Gnuplot* (Williams et al., 2010) and *Visit* (Childs et al., 2012). The authors want to thank D. Fuster, S. Mercier and the anonymous reviewers for helpful discussions, corrections and suggestions that have helped us improve the paper. W. Aniszewski thanks A.A.S. for proofreading the manuscript.

References

Aniszewski, W., 2011. Large eddy simulation of turbulent two-phase flow. Ph.D. thesis, Czestochowa University of Technology, Czestochowa, Poland.

Aniszewski, W., Ménard, T., Marek, M., 2014. Volume of Fluid (VOF) type advection methods in two-phase flow: A comparative study. Comput. Fluids 97 (0), 52–73.

Batchelor, G., 1967. An introduction to fluid dynamics. Cambridge University Press.

Caflisch, R., Miksis, M., Papanicolaou, G., Ting, L., 1985. Effective equations for wave propagation in bubbly liquids. J. Fluid Mech. 153, 259–273.

Carnahan, B., Luther, H., Wilkes, J., 1969. Applied Numerical Methods. John Wiley & Sons, Inc., New York.

Childs, H., Brugger, E., Whitlock, B., Meredith, J., Ahern, S., Pugmire, D., Biagas, K., Miller, M., Harrison, C., Weber, G. H., Krishnan, H., Fogal, T., Sanderson, A., Garth, C., Bethel, E. W., Camp, D., Rübel, O., Durant, M., Favre, J. M., Navrátil, P., Oct 2012. VisIt: An End-User Tool For Visualizing and Analyzing Very Large Data. In: High Performance Visualization–Enabling Extreme-Scale Scientific Insight. pp. 357–372.

Cummins, S., Francois, M., Kothe, D., 2004. Estimating curvature from volume fractions. Comput. Struct. 83 (6–7), 425–434.

de Rességuier, T., Signor, L., Dragon, A., Roy, G., 2010. Dynamic fragmentation of laser shock-melted tin: experiment and modelling. Int. J. Fracture 163 (1–2), 109–119.

Everitt, S., Harlen, O., Wilson, H., 2006. Competition and interaction of polydisperse bubbles in polymer foams. J. Non-Newt. Fluid 137 (1–3), 60–71.

Falgout, R., Yang, U., 2002. hypre: a library of high performance preconditioners. In: Sloot, P., Hoekstra, A., Tan, C., Dongara, J. (Eds.), Computational Science – ICCS 2002. Vol. 2331 of Lect. Notes Comput. Sc. Springer, pp. 632–641.

Girifalco, L. A., 2000. Statistical Mechanics of Solids. Oxford University Press, New York.

Hirth, C., Nichols, B., 1981. Volume of Fluid (VOF) method for the dynamics of free boundaries. J. Comput. Phys. 39 (1), 201–225.

Ilinskii, Y., Hamilton, M., Zabolotskaya, E., 2007. Bubble interaction dynamics in Lagrangian and Hamiltonian mechanics. J. Acoust. Soc. Am. 121 (2), 786–795.

Li, J., 1995. Calcul d'interface affine par morceaux. C.R. Acad. Sci. II B 320 (8), 391–396.

Ling, Y., Zaleski, S., Scardovelli, R., 2015. Multiscale simulation of atomization with small droplets represented by a Lagrangian point-particle model. Int. J. Multiphas. Flow 76, 122–143.

López, J., Hernández, J., Gómez, P., Faura, F., 2005. An improved plic-vof method for tracking thin fluid structures in incompressible two-phase flows. Journal of Computational Physics 208 (1), 51 – 74.
URL http://www.sciencedirect.com/science/article/pii/S0021999105000513

Malan, L., Ling, Y., Scardovelli, R., Llor, A., Zaleski, S., 2018. Direct numerical simulations of pore competition in idealized micro-spall using the VOF method. Comput. Fluids (submitted) also available as arXiv:1711.04561 [physics.flu-dyn].

Malan, L., Zaleski, S., 2015. Numerical simulation of bubble competition during micro-spalling. Tech. Rep. 13-39-C-DSPG/CAJ, Institut Jean le Rond d'Alembert.

Marek, M., Aniszewski, W., Boguslawski, A., 2008. Simplified volume of fluid method (SVOF) for two-phase flows. TASK quaterly 12, 255–265.

Ménard, T., Tanguy, S., Berlemont, A., 2007. Coupling level set/ volume of fluid/ ghost fluid methods, validation and application to 3d simulation of the primary breakup of a liquid jet. International Journal of Multiphase Flows 33, 510–524.

Pilliod, J., Puckett, E., 2004. Second order accurate volume of fluid algorithms for tracking material interfaces. Journal of Computational Physics 1999, 465–502.

Popinet, S., 2003. Gerris: a tree-based adaptive solver for the incompressible Euler equations in complex geometries. J. Comput. Phys. 190 (2), 572–600.

Qiu, T., Xiong, Y., Xiao, S., Li, X., Hu, W., Deng, H., 2017. Non-equilibrium molecular dynamics simulations of the spallation in ni: Effect of vacancies. Computational Materials Science 137, 273 – 281.
URL http://www.sciencedirect.com/science/article/pii/S0927025617302793

Salvador, F., S., R., Crialesi-Esposito, M., Blanquer, I., 2018. Analysis on the effects of turbulent inflow conditions on spray primary atomization in the near-field by direct numerical simulation. International Journal of Multiphase Flow 102, 49 – 63.

Scardovelli, R., Zaleski, S., 2000. Analytical relations connecting linear interfaces and volume fractions in rectangular grids. J. Comput. Phys. 164 (1), 228–237.

Shu, C.-W., 1997. Essentially Non-Oscillatory and Weighted Essentially Non-Oscillatory schemes for hyperbolic conservation laws. Tech. Rep. CR-97-206253, NASA.

Signor, L., de Rességuier, T., Dragon, A., Roy, G., Fanget, A., Faessel, M., 2010. Investigation of fragments size resulting from dynamic fragmentation in melted state of laser shock-loaded tin. Int. J. of Impact Eng. 37 (8), 887–900.

Sweby, P., 1984. High resolution schemes using flux limiters for hyperbolic conservation laws. SIAM J. Numer. Anal. 21 (5), 995–1011.

Tryggvason, G., Scardovelli, R., Zaleski, S., 2011. Direct numerical simulations of gas–liquid multiphase flows. Cambridge University Press.

Vaudor, G., Ménard, T., Aniszewski, W., Berlemont, A., 2017. A consistent mass and momentum flux computation method for two phase flows. application to atomization process. Computers and Fluids 152, 204–216.

Wang, K., Xiao, S., Deng, H., Zhu, W., Hu, W., 2014. An atomic study on the shock-induced plasticity and phase transition for iron-based single crystals. International Journal of Plasticity 59, 180 – 198.
URL http://www.sciencedirect.com/science/article/pii/S0749641914000503

Williams, T., Kelley, C., many others, March 2010. Gnuplot 4.4: an interactive plotting program. http://gnuplot.sourceforge.net/.

Xiao, F., Ii, S., Chen, C., 2011. Revisit to the THINC scheme: A simple algebraic vof algorithm. Journal of Comput. Physics 230, 7086–7092.

Youngs, D., 1984. Numerical simulation of turbulent mixing by Rayleigh–Taylor instability. Fronts, Interfaces and Patterns, 32.